

# A generalized theory of flow forcing by rough topography

Timour Radko<sup>†</sup>

Department of Oceanography, Naval Postgraduate School, Monterey, CA 93943, USA

(Received 3 December 2022; revised 20 February 2023; accepted 21 February 2023)

---

An analytical model is developed which explores the impact of irregular sea-floor roughness on large-scale oceanic flows. The previously reported asymptotic ‘sandpaper’ theory of flow-topography interaction represents relatively swift currents and exhibits singular behaviour in the weak flow limit. The present investigation systematically spans a wider parameter space and identifies the principal dissimilarities in the topographic regulation of slow and fast currents. The fast flows are controlled by the Reynolds stresses produced by topographically generated eddies. In contrast, relatively weak flows are more affected by the eddy-induced bottom form drag. The asymptotic models for fast and slow currents are then combined to arrive at a concise description of flow forcing by small-scale topography in homogeneous and multilayer models. The proposed closure is validated by comparing corresponding topography-resolving and parametric simulations.

**Key words:** ocean circulation, topographic effects

---

## 1. Introduction

It is hard to name any other branch of oceanography that would enjoy such persistent interest and broad acceptance of its significance but, at the same time, would remain as underexplored as the flow-topography interaction theory. Particularly nascent is our understanding of processes induced by the sea-floor roughness, defined here as bathymetric features with a lateral extent of several kilometres. Rough topography affects several aspects of ocean circulation. It tends to suppress baroclinic instability, thereby controlling the intensity of mesoscale variability in the ocean (LaCasce *et al.* 2019; Radko 2020). Sea-floor roughness extends the lifespan of coherent vortices (Gulliver & Radko 2022), enhancing their ability to transport heat, salt, and nutrients. On a more conceptual level, rough topography could be the key to one of the most fundamental problems in geophysical fluid dynamics, the explanation of the direct cascade of energy and thermal variance. Mechanical and thermodynamic forcing at the sea surface occurs on the scales

<sup>†</sup> Email address for correspondence: [tradko@nps.edu](mailto:tradko@nps.edu)

of ocean basins, whereas the energy and thermal variance are ultimately dissipated by molecular processes acting on the microscale (Wunsch & Ferrari 2004; Merryfield 2005). The small-scale eddies generated by rough topography could dynamically connect microstructure with larger scales of motion (Dewar & Hogg 2010; Dewar, Berloff, & Hogg 2011) and, therefore, investigations of flow-topography interactions may lead to essential insights into global energetics.

While there is little doubt about the overall importance of sea-floor roughness, a consistent view of the specific mechanisms at play – and their relative impact on large-scale patterns – is only beginning to emerge. Traditionally, much attention has been paid to the effects of topographic pressure torque (Hughes & de Cuevas 2001; Jackson, Hughes, & Williams 2006; Stewart, McWilliams, & Solodoch 2021), with particular emphasis on lee-wave drag (Naveira Garabato *et al.* 2013; Eden, Olbers, & Eriksen 2021; Klymak *et al.* 2021). Several observable phenomena are caused by the topographic steering of low Rossby number flows (Marshall 1995; Wählin 2002). It is manifested, for instance, in the formation of stationary Taylor columns that trap fluid above salient topographic features (Taylor 1923; Johnson 1978). Yet another distinct mechanism of topographic control involves small-scale eddies generated by large-scale currents interacting with rough bathymetry. These eddies produce Reynolds stresses that, in turn, influence primary flows. Several examples of such dynamics were presented by Holloway (1987, 1992), who argued that the interaction between topography and eddies can, in some cases, reinforce primary circulation patterns. In other systems, the topographic eddy stresses tend to substantially slow down abyssal currents (Radko 2020; Gulliver & Radko 2022).

One of the key objectives of the flow-topography interaction theory is the development of explicit closure models representing the impact of sea-floor roughness on large-scale flows. The pragmatic motivation for this effort is related to the resolution limitations of general circulation models. Despite advancements in high-performance computing, roughness-resolving global models will not be used for extended climate simulations in the foreseeable future. Thus, parameterizing the effects of small-scale bathymetry is the most promising way forward. Adopting topographic closure models also enhances the prospects of finding analytical solutions that conceptualize large-scale oceanic phenomena affected by sea-floor roughness. Finally, as our study illustrates, the very process of developing such parameterizations can be highly effective in terms of explaining the essential dynamics at work.

In the present investigation, closure models for sea-floor roughness are developed using techniques of multiscale analysis, a broad and active field with numerous fluid-dynamical applications (e.g. Meshalkin & Sinai 1961; Manfroi & Young 1999, 2002; Balmforth & Young, 2002, 2005; Mei & Vernescu 2010). The principal idea of multiscale methods involves rewriting the governing equations using two sets of independent variables. In our case, large scales describe primary flows, and small ones are based on the lateral extent of topographic features that the model strives to parameterize. The crux of this approach is the derivation of solvability conditions that describe the system entirely on large scales. Strictly speaking, the theory assumes scale separation between the primary flow components and those induced by rough topography. It is unclear how well this assumption describes nature, but we assume and subsequently verify that the resulting analytical model reflects behaviours that hold even without the scale separation. Our earlier results in this area (e.g. Radko & Kamenkovich 2017; Radko 2020, 2022a,b) also indicate that multiscale models perform remarkably well for a wide range of systems, including those in which the lines between large and small scales are blurred.

Traditionally, multiscale methods have been applied to simple analytical small-scale patterns (e.g. Gama, Vergassola, & Frisch 1994; Novikov & Papanicolau 2001;

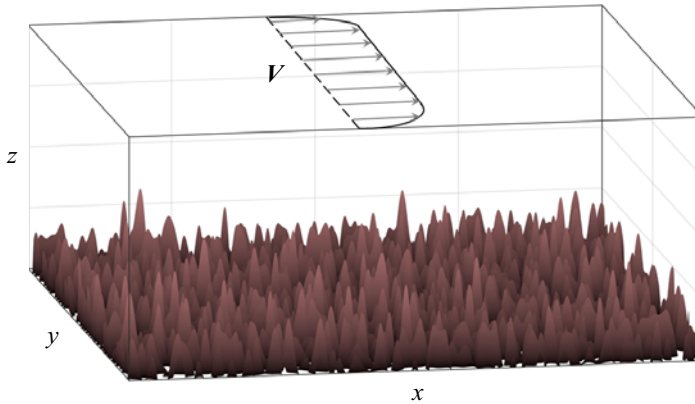


Figure 1. Schematic diagram illustrating the set-up of the sandpaper model. A large-scale flow interacts with irregular sea floor, the pattern of which conforms to the Goff & Jordan (1988) spectrum.

Radko 2011*a,b*), ultimately leading to explicit large-scale equations. In the context of flow-topography interaction problems, analytical progress has been made for one-dimensional sinusoidal bathymetry (e.g. Benilov 2000, 2001; Vanneste 2003; Radko 2020). The representation of more realistic irregular two-dimensional topographic features is more challenging and explicit solutions have mostly been derived for special cases (e.g. Vanneste 2000; Goldsmith & Esler 2021). The fundamental limitation of such models is their inherently qualitative connection to the observed or simulated phenomena.

Fortunately, a recent advancement opened the path for analytical treatments of realistic patterns of small-scale topography. Radko (2022*a,b*) pointed out that multiscale methods can be effectively applied to irregular bathymetry, provided that its statistical spectral representation is known. The key step is the application of Parseval's theorem (Parseval 1806), equating the spatial average of any quadratic quantity to integrals of Fourier coefficients in wavenumber space. This link proved to be critical since ocean depth variability is adequately represented by the observationally derived spectrum of Goff & Jordan (1988). The resulting framework was termed the sandpaper model, a nickname invoking associations with small, irregular, tightly packed particles of sandpaper – features that are reminiscent of rough bathymetry in the ocean (figure 1). The sandpaper model has led to an explicit representation of flow forcing by rough topography, essentially yielding a rigorous asymptotics-based parameterization.

The previous versions of the sandpaper model (Radko 2022*a,b*) were successfully tested for oceanographically relevant parameters on the canonical vortex spin-down problem. These works, however, have also raised several fundamental questions that the present investigation attempts to address. The primary concern is the generality of the proposed solutions. The models of Radko (2022*a,b*) explored a specific sector in the multidimensional parameter space characterized by rapid flows with asymptotically large Reynolds numbers. However, there are clear signs that the solutions obtained for this regime are not universal. For instance, the expressions for topographic forcing derived by Radko (2022*a,b*) are inversely proportional to large-scale velocity. This singularity suggests that forcing unphysically increases without bound with decreasing flow speed – a tell-tale sign that a different asymptotic model is needed to capture the limit of weak large-scale currents.

To explore a wider range of parameters and ultimately develop a general model of topographic forcing, we consider an asymptotic sector corresponding to slow flows

with low Reynolds numbers. The properties of fast- and slow-flow models turned out to be fundamentally different. For instance, the fast-flow regime (Radko, 2022a,b) is characterized by the profound influence of the Reynolds stresses produced by the interaction of large-scale currents with rough bathymetry. Slow currents, on the other hand, are controlled by the eddy-induced form drag, and in this limit, the large-scale forcing by rough topography is proportional to large-scale velocity. To offer a more universal description of the flow field, we propose a hybrid closure for sea-floor roughness that converges to the corresponding asymptotic expressions in the limits of fast and slow currents. In contrast to the earlier parameterizations of Radko (2022a,b), which required an *ad hoc* regularization for weak large-scale flows, the hybrid model is well behaved and can be readily implemented in large-scale evolutionary equations.

The material is organized as follows. The governing equations for the homogeneous model are described in § 2. Section 3 presents the asymptotic multiscale theory that leads to an explicit closure for small-scale bathymetry. The analytical model is validated by roughness-resolving simulations in § 4. The extension of the asymptotic analysis to the multilayer framework is discussed in § 5. The results are summarized, and conclusions are drawn, in § 6.

## 2. The homogeneous model

Our starting point is the homogeneous quasi-geostrophic rigid-lid model (e.g. Pedlosky 1987)

$$\frac{\partial \nabla^2 \psi^*}{\partial t^*} + J(\psi^*, \nabla^2 \psi^*) + \beta^* \frac{\partial \psi^*}{\partial x^*} + \frac{f_0^*}{H_0^*} J(\psi^*, \eta^*) = \nu^* \nabla^4 \psi^* - \gamma^* \nabla^2 \psi^*, \quad (2.1)$$

where  $\psi^*$  is the streamfunction associated with the velocity field  $(u^*, v^*) = (-\partial \psi^* / \partial y^*, \partial \psi^* / \partial x^*)$ ,  $\eta^*$  is the depth variation,  $J$  is the Jacobian,  $\nu^*$  is the lateral eddy viscosity and  $\gamma^*$  is the Ekman bottom drag coefficient. Also,  $H_0^*$  and  $f_0^*$  are the reference values of the ocean depth and the Coriolis parameters, respectively, and  $\beta^* \equiv \partial f^* / \partial y^*$  is the meridional gradient of planetary vorticity. The asterisks represent dimensional quantities.

We explore the impact of topographic patterns with the lateral extent  $O(L^*)$  on large-scale flows with scales  $O(L_{LS}^*)$ . We assume that fine topographic scales are limited to a finite range  $[L_{min}^*, L_C^*]$ , where  $L_C^*$  is the cutoff wavelength formally separating small and large scales. The lower bound ( $L_{min}^*$ ) is introduced to ensure that all relevant Rossby numbers are low – the key assumption of the quasi-geostrophic framework. This leads to the following ordering of spatial scales:

$$\frac{U^*}{f_0^*} \ll L_{min}^* < L^* < L_C^* \ll L_{LS}^*, \quad (2.2)$$

where  $U^*$  is the velocity scale. The number of controlling parameters is reduced by non-dimensionalizing (2.1) using  $1/f_0^*$  and  $L^*$  as the units of time and lateral extent, respectively,

$$\psi^* = f_0^* L^{*2} \psi, \quad x^* = L^* x, \quad y^* = L^* y, \quad t^* = \frac{t}{f_0^*}. \quad (2.3)$$

The topographic height, however, is non-dimensionalized as

$$\eta^* = H_0^* \eta. \quad (2.4)$$

To be specific, we consider the oceanographically relevant scales of

$$L^* = 10^4 \text{ m}, \quad H_0^* = 4000 \text{ m}, \quad f_0^* = 10^{-4} \text{ s}^{-1}. \quad (2.5)$$

The non-dimensionalization reduces the governing equation (2.1) to

$$\frac{\partial \nabla^2 \psi}{\partial t} + J(\psi, \nabla^2 \psi) + \beta \frac{\partial \psi}{\partial x} + J(\psi, \eta) = \nu \nabla^4 \psi - \gamma \nabla^2 \psi, \quad (2.6)$$

where

$$\beta = \frac{\beta^* L^*}{f_0^*}, \quad \nu = \frac{\nu^*}{f_0^* L^{*2}}, \quad \gamma = \frac{\gamma^*}{f_0^*}. \quad (2.7)$$

To explore the interaction between flow components of large and small lateral extents, we introduce the scale-separation parameter

$$\varepsilon = \frac{L_C^*}{L_S^*} \ll 1. \quad (2.8)$$

This parameter is used to define the new set of spatial scales  $(X, Y)$  that reflect the dynamics of large-scale processes. These variables are related to the original ones through

$$(X, Y) = \varepsilon(x, y). \quad (2.9)$$

The derivatives in the governing system (2.6) are replaced accordingly

$$\frac{\partial}{\partial x} \rightarrow \frac{\partial}{\partial X} + \varepsilon \frac{\partial}{\partial x}, \quad \frac{\partial}{\partial y} \rightarrow \frac{\partial}{\partial Y} + \varepsilon \frac{\partial}{\partial y}. \quad (2.10)$$

Topographic patterns considered in the sandpaper model vary on both large and small scales

$$\eta = \eta_L(X, Y) + \eta_S(x, y). \quad (2.11)$$

A natural way to separate bathymetry into the small- and large-scale components (Radko 2022a,b) is based on the Fourier transform of  $\eta$

$$\eta = \frac{\sqrt{L_x L_y}}{2\pi} \iint \tilde{\eta}(k, l) \exp(ikx + ily) dk dl, \quad (2.12)$$

where  $(k, l)$  are the wavenumbers in  $x$  and  $y$ , respectively, tildes hereafter denote Fourier images and  $(L_x, L_y)$  is the domain size. Since the Fourier transform is linear, it can be conveniently separated into the contributions from high and low wavenumbers as follows:

$$\begin{aligned} \eta &= \underbrace{\frac{\sqrt{L_x L_y}}{2\pi} \iint_{\kappa < 2\pi/L_C} \tilde{\eta}(k, l) \exp(ikx + ily) dk dl}_{\eta_L} \\ &+ \underbrace{\frac{\sqrt{L_x L_y}}{2\pi} \iint_{\kappa > 2\pi/L_C} \tilde{\eta}(k, l) \exp(ikx + ily) dk dl}_{\eta_S}, \end{aligned} \quad (2.13)$$

where  $\kappa \equiv \sqrt{k^2 + l^2}$ . The  $\eta_L$  component in (2.13) gently varies on large scales, and  $\eta_S$  represents small-scale variability. The normalization factor  $\sqrt{L_x L_y}/2\pi$  in the definition of

the Fourier transform is introduced to ensure that the Parseval identity (Parseval 1806), to be used in subsequent developments, takes a convenient form

$$\langle ab \rangle_{x,y} = \iint \tilde{a} \cdot \text{conj}(\tilde{b}) \, dk \, dl. \tag{2.14}$$

Angle brackets hereafter represent mean values, with the averaging variables listed in the subscript.

### 3. The multiscale analysis

We now explore flow-topography interactions using methods of multiscale mechanics. Our earlier efforts in this area (Radko 2022a,b) have led to a consistent treatment of relatively swift flows. However, the resulting theory was inapplicable for weak currents, motivating the development of an analogous slow-flow model. To highlight the principal differences and similarities between the two systems, we first review the key features of the fast-flow model.

#### 3.1. Rapid flows

The barotropic sandpaper theory (Radko, 2022a) was based on the expansion in small parameter  $\varepsilon$  quantifying the disparity of large and small spatial scales (2.8). The flow was assumed to be inviscid at the leading order with

$$Re = \frac{U^* L^*}{\nu^*} = O(\varepsilon^{-1}). \tag{3.1}$$

Nevertheless, even weak friction proved to be critical due to the catalytic nature of rough topography, which amplified the effects of explicit dissipation by as much as 2–3 orders of magnitude. The expansion opened with a large-scale flow  $\bar{\psi}(X, Y, t)$  and its first-order correction was represented by a small-scale pattern  $\psi_S(x, y)$ . The dynamics of this perturbation was controlled by the homogenization of small-scale potential vorticity (PV), with  $\psi_S$  rigidly controlled by topography and satisfying

$$\nabla^2 \psi_S + \eta_S(x, y) = 0. \tag{3.2}$$

The closed evolutionary equation for  $\bar{\psi}$  was obtained as a solvability condition by averaging the governing equation in small-scale variables. In terms of original variables (2.9), the  $\bar{\psi}$  equation takes the form

$$\frac{\partial}{\partial t} \nabla^2 \bar{\psi} + J(\bar{\psi}, \nabla^2 \bar{\psi} + \eta_L) + \beta \frac{\partial \bar{\psi}}{\partial x} + D_{fast} + \gamma \nabla^2 \bar{\psi} = \nu \nabla^4 \bar{\psi}, \tag{3.3}$$

where  $D_{fast}$  represents cumulative effects of rough bathymetry. It originates from the averaged nonlinear advective term  $\langle J(\psi', \nabla^2 \psi') \rangle_{x,y}$  in the governing vorticity equation, where  $\psi' = \psi - \bar{\psi}$ , and represents the eddy-induced mixing of momentum. Interestingly, the topographic form drag does not affect the large-scale circulation at the leading order.

In this fast-flow regime, topographic forcing reduces to

$$D_{fast} = G_{fast} \left( \frac{\partial}{\partial x} \left( \frac{\bar{v}}{\bar{u}^2 + \bar{v}^2} \right) - \frac{\partial}{\partial y} \left( \frac{\bar{u}}{\bar{u}^2 + \bar{v}^2} \right) \right), \quad (3.4)$$

where  $(\bar{u}, \bar{v}) = (-\partial\bar{\psi}/\partial y, \partial\bar{\psi}/\partial x)$ . The coefficient  $G_{fast}$  in (3.4) is fully determined by the spectrum of small-scale topography and the explicit dissipation parameters

$$G_{fast} = 2\pi \int |\tilde{\eta}_S|^2 \left( \frac{\gamma}{\kappa} + \nu\kappa \right) d\kappa, \quad \kappa = \sqrt{k^2 + l^2}, \quad (3.5)$$

where  $\tilde{\eta}_S$  is the Fourier image of the statistically isotropic small-scale component of topography. In essence, this theory parameterizes the effects of sea-floor roughness on larger scales of motion. However, the parameterization is derived directly from governing equations without invoking any empirical assumptions, commonly used by other closure models. The benefits brought by the sandpaper model include the opportunity to perform efficient numerical experiments without having to resolve small-scale features of the bottom relief if the spectrum of topography is known.

Unfortunately, there is one feature that seems unphysical and complicates the direct implementation of (3.3)–(3.5) in numerical models – the unbounded increase of (3.4) in the weak flow limit:  $\bar{V} \equiv \sqrt{\bar{u}^2 + \bar{v}^2} \rightarrow 0$ . Radko (2022a,b) has dealt with this inconvenience by constraining  $D_{fast}$  in low-speed regions. While such regularization served the immediate purpose, making it possible to perform parametric simulations, its *ad hoc* character brought a certain sense of dissatisfaction. It implied that the model failed to capture the dynamics of weak flows, and the following analysis seeks to rectify this deficiency.

### 3.2. Weak flows

To offer an analogous description of the slow-flow limit, we now consider a regime in which Reynolds numbers are asymptotically small

$$Re = \frac{U^*L^*}{\nu^*} = O(\varepsilon). \quad (3.6)$$

This limit is captured by the expansion that opens with the  $O(\varepsilon)$  large-scale pattern

$$\bar{\psi} = \varepsilon\psi^{(1)}(X, Y, T). \quad (3.7)$$

The governing parameters are rescaled as follows:

$$\beta = \varepsilon^4\beta_0, \quad \gamma = \varepsilon^3\gamma_0, \quad \nu = \varepsilon\nu_0, \quad \eta_S = \varepsilon^2\eta_{S0}, \quad \eta_L = \varepsilon^3\eta_{L0}, \quad (3.8)$$

which affords the inclusion of all relevant effects in the evolutionary equation and broadly reflects the typical values of parameters in the oceanographic context. The temporal evolution in this regime is controlled by relatively slow processes driven by explicit dissipation. Hence, the temporal variable is rescaled as  $T = \varepsilon^3t$ , and the time derivative in the governing system (2.6) is replaced accordingly

$$\frac{\partial}{\partial t} \rightarrow \varepsilon^3 \frac{\partial}{\partial T}. \quad (3.9)$$

The interaction of the large-scale flow with low-amplitude rough topography forces the small-scale streamfunction response at  $O(\varepsilon^3)$  and the asymptotic series are extended

accordingly

$$\psi = \varepsilon\psi^{(1)}(X, Y, T) + \varepsilon^3\psi^{(3)}(X, Y, x, y, T) + O(\varepsilon^4). \tag{3.10}$$

Series (3.10) are then substituted in the governing equation (2.6) and terms of the same order in  $\varepsilon$  are collected. The leading-order balance is realized at  $O(\varepsilon^4)$

$$\frac{\partial\psi^{(1)}}{\partial X} \frac{\partial\eta_{S0}}{\partial y} - \frac{\partial\psi^{(1)}}{\partial Y} \frac{\partial\eta_{S0}}{\partial x} = \nu_0\nabla^4\psi^{(3)}. \tag{3.11}$$

The  $O(\varepsilon^5)$  balance plays no role in the model development and is not listed here. The key solvability condition leading to the evolutionary equation for  $\bar{\psi}$  is obtained by averaging the  $O(\varepsilon^6)$  balance in  $(x, y)$

$$\frac{\partial\zeta^{(1)}}{\partial T} + J_{X,Y}(\psi^{(1)}, \zeta^{(1)} + \eta_{L0}) + \beta_0 \frac{\partial\psi^{(1)}}{\partial X} + D_{slow\ 0} + \gamma_0\zeta^{(1)} = \nu_0 \left( \frac{\partial^2\zeta^{(1)}}{\partial X^2} + \frac{\partial^2\zeta^{(1)}}{\partial Y^2} \right), \tag{3.12}$$

where  $\zeta^{(1)} \equiv \partial^2\psi^{(1)}/\partial X^2 + \partial^2\psi^{(1)}/\partial Y^2$  and

$$D_{slow\ 0} = \left\langle \frac{\partial\psi^{(3)}}{\partial X} \frac{\partial\eta_{S0}}{\partial y} - \frac{\partial\psi^{(3)}}{\partial Y} \frac{\partial\eta_{S0}}{\partial x} \right\rangle_{x,y}. \tag{3.13}$$

Here,  $D_{slow\ 0}$  represents the topographic forcing of large-scale flows by rough bathymetry. It originates from the term  $\langle J(\psi', \eta_S) \rangle_{x,y}$  in the governing vorticity equation and represents the eddy-induced form drag. In contrast to the fast-flow regime (§ 3.1), the Reynolds stress does not affect the system evolution at this order.

To express  $D_{slow\ 0}$  in terms of properties of the large-scale flow, we eliminate  $\psi^{(3)}$  between (3.11) and (3.13). This procedure is relegated to Appendix A, and the result is an explicit expression for  $D_{slow\ 0}$  in (A13). The final step in the model development is the transition to the original un-rescaled variables, which reduces (3.12) to

$$\frac{\partial}{\partial t} \nabla^2 \bar{\psi} + J(\bar{\psi}, \nabla^2 \bar{\psi} + \eta_L) + \beta \frac{\partial \bar{\psi}}{\partial x} + D_{slow} + \gamma \nabla^2 \bar{\psi} = \nu \nabla^4 \bar{\psi}, \tag{3.14}$$

where

$$D_{slow} = \varepsilon^6 D_{slow\ 0} = G_{slow} \nabla^2 \bar{\psi}, \quad G_{slow} = \pi \int \frac{|\tilde{\eta}_S|^2}{\nu\kappa} d\kappa. \tag{3.15}$$

It should be emphasized that the relations between the topographic forcing and the current speed in the fast-flow and slow-flow models are fundamentally different. In fast flows, the topographic drag decreases with increasing speed, but in slow ones, it increases. This dissimilar behaviour motivates the development of a hybrid model that captures the transition between the two regimes and is readily implementable in numerical models.

### 3.3. Hybrid model

Two thousand years ago, Aristotle famously wrote ‘A whole is that which has a beginning, middle, and end’. If we apply the same principle to the sandpaper theory, it becomes clear that capturing the beginning (§ 3.2) and the end (§ 3.1) of the velocity range would still leave our model incomplete, unless the middle part is properly represented. Thus, we now



proceed with the development of the whole theory, but in doing so, we insist that the design of the transitional model is consistent with both the ‘beginning’ and the ‘end’.

To formulate the hybrid model, we note that the expressions for the topographic forcing in both fast-flow and slow-flow limits can be written as

$$D = \text{curl}(\mathbf{M}). \quad (3.16)$$

Vector  $\mathbf{M}$  can be interpreted as the topographic momentum forcing. Its fast and slow limits are defined as follows:

$$\mathbf{M}_{fast} = G_{fast} \bar{V}^{-1} \mathbf{s}, \quad \mathbf{M}_{slow} = G_{slow} \bar{V} \mathbf{s}, \quad (3.17)$$

where  $\mathbf{s} \equiv (\bar{u} \bar{V}^{-1}, \bar{v} \bar{V}^{-1})$  is the unit vector aligned with the large-scale flow.

The structural similarity of the expressions in (3.17) suggests a natural design of the hybrid model. We introduce an analytical function  $F(\bar{V})$  that asymptotes to  $G_{slow} \bar{V}$  and  $G_{fast} \bar{V}^{-1}$  in the limits of low and high velocities, respectively. The momentum forcing is then represented accordingly

$$\mathbf{M}_{hybrid} = F(\bar{V}) \mathbf{s}. \quad (3.18)$$

To construct the appropriate function  $F(\bar{V})$ , we first estimate the critical velocity  $V_C$  that marks the transition between the fast-flow and slow-flow regimes. This is accomplished by considering the crossing point of the two asymptotic models

$$D_{slow}(V_C) = D_{fast}(V_C), \quad (3.19)$$

which leads to

$$V_C = \sqrt{\frac{G_{fast}}{G_{slow}}}. \quad (3.20)$$

This point of transition is determined by the intensity of dissipative processes. For systems in which small-scale dissipation is controlled by lateral viscosity, we arrive at the scaling

$$V_C \sim \nu \kappa_\eta, \quad (3.21)$$

where  $\kappa_\eta$  is the dominant wavenumber of rough topography. The dimensional counterpart of (3.21) is equally remarkable in its simplicity:  $V_C^* \sim \nu^* \kappa_\eta^*$ .

The proposed model for  $F$ , which reflects the regime transition at  $\bar{V} = V_C$ , is defined by

$$\ln(FF_C^{-1}) = -\sqrt{a^2 + \ln^2(\bar{V}V_C^{-1})}, \quad (3.22)$$

where  $F_C \equiv \sqrt{G_{fast}G_{slow}}$  and  $a$  is an adjustable parameter. For  $\bar{V} \gg V_C$ , the right-hand side of (3.22) can be approximated by  $-\ln(\bar{V}V_C^{-1})$ , which implies that  $F \approx G_{fast} \bar{V}^{-1}$ . For  $\bar{V} \ll V_C$ , the leading-order balance of (3.22) becomes  $\ln(FF_C^{-1}) \approx \ln(\bar{V}V_C^{-1})$  and  $F \approx G_{slow} \bar{V}$ . Parameter  $a$  in (3.22) controls the width of the intermediate region connecting the slow and fast regimes. For small values of  $a$ , the transition is rapid and a relatively minor variation in velocity can shift the system into the opposite regime. If  $a$  is large, the transition is gentler, and the intermediate region is wide. Numerical simulations, some of which will be presented in § 4, indicate that the intermediate zone tends to be relatively

narrow, with only one order of magnitude separating clearly fast and clearly slow flows. These features are well represented by

$$a = 1, \tag{3.23}$$

which will be used in all subsequent calculations. The topographic momentum forcing (3.18) in this case becomes

$$\mathbf{M}_{hybrid} = F_C \exp\left(-\sqrt{1 + \ln^2(\bar{V}V_C^{-1})}\right) \mathbf{s}. \tag{3.24}$$

The corresponding  $D$ -term takes the form

$$D_{hybrid} = \frac{\partial}{\partial x} \left[ \bar{v} \bar{V}^{-1} F_C \exp\left\{-\sqrt{1 + \ln^2(\bar{V}V_C^{-1})}\right\}\right] - \frac{\partial}{\partial y} \left[ \bar{u} \bar{V}^{-1} F_C \exp\left\{-\sqrt{1 + \ln^2(\bar{V}V_C^{-1})}\right\}\right], \tag{3.25}$$

which makes it possible to represent the effects of small-scale topography by adopting the parametric model

$$\frac{\partial}{\partial t} \nabla^2 \bar{\psi} + J(\bar{\psi}, \nabla^2 \bar{\psi} + \eta_L) + \beta \frac{\partial \bar{\psi}}{\partial x} + D_{hybrid} + \gamma \nabla^2 \bar{\psi} = \nu \nabla^4 \bar{\psi}. \tag{3.26}$$

### 3.4. The energetics

The coefficients of the fast and slow drag laws,  $G_{slow}$  and  $G_{fast}$ , were obtained previously (e.g. § 3.2) by performing formal multiscale expansions. However, a simpler and perhaps more intuitive derivation can also be offered by considering the energetics of the flow-topography interaction as follows.

For both slow and fast flows, the energy equation can be derived directly from the original vorticity equation by multiplying (2.6) by  $\psi$  and averaging the result in  $x$  and  $y$ . For simplicity, we focus on lateral dissipation and ignore the Ekman bottom drag, which results in

$$\frac{\partial E}{\partial t} = -\nu \langle \psi \nabla^4 \psi \rangle_{x,y} \approx -\nu \langle \psi_S \nabla^4 \psi_S \rangle_{x,y}, \tag{3.27}$$

where  $E = \frac{1}{2} \langle |\nabla \psi|^2 \rangle_{x,y}$ . In (3.27), we assume that the energy is dissipated most effectively by small-scale patterns produced by topography. One can similarly derive an energy equation for the parametrized models

$$\frac{\partial \bar{E}}{\partial t} = -\langle D \bar{\psi} \rangle_{x,y}, \tag{3.28}$$

where  $\bar{E} = \frac{1}{2} \langle |\nabla \bar{\psi}|^2 \rangle_{x,y}$ . The crux of the energy-based approach is the requirement that parametric models properly represent the net energy loss, which leads to

$$\langle D \bar{\psi} \rangle_{x,y} = \nu \langle \psi_S \nabla^4 \psi_S \rangle_{x,y}. \tag{3.29}$$

For the slow-flow model, the parameterization is sought in the form

$$D = G_{slow} \nabla^2 \bar{\psi}, \tag{3.30}$$

and the dominant balance is

$$\frac{\partial \bar{\psi}}{\partial x} \frac{\partial \eta}{\partial y} - \frac{\partial \bar{\psi}}{\partial y} \frac{\partial \eta}{\partial x} = \nu \nabla^4 \psi_S. \tag{3.31}$$

The counterparts of (3.30) and (3.31) in the fast-flow model are

$$D = G_{fast} \nabla \left( \frac{\nabla \bar{\psi}}{|\nabla \bar{\psi}|^2} \right), \quad \eta = -\nabla^2 \psi_S. \quad (3.32)$$

When (3.29) is combined with (3.30) and (3.31) under the assumption that  $\partial \bar{\psi} / \partial x$  and  $\partial \bar{\psi} / \partial y$  do not contain small scales, we arrive at  $G_{slow} = (\pi/\nu) \int (|\bar{\eta}_S|^2/\kappa) d\kappa$ . Likewise, combining (3.29) and (3.32) yields  $G_{fast} = 2\pi\nu \int |\bar{\eta}_S|^2 \kappa d\kappa$ . Both results are fully consistent with the formal asymptotic expansion for  $\gamma = 0$ .

#### 4. Validation

##### 4.1. The set-up of experiments

We now assess the performance characteristics of all three models – fast flow, slow flow and hybrid – using topography-resolving simulations. The numerical configuration is illustrated in figure 1. The model is initiated with zonal large-scale flow, the speed of which varies in  $y$ . The sea floor is irregular and conforms to the observationally derived spectrum of Goff & Jordan (1988)

$$P_\eta^* = \frac{h^{*2}(\mu - 2)}{(2\pi)^3 k_0^* l_0^*} \left( 1 + \left( \frac{k^*}{2\pi k_0^*} \right)^2 + \left( \frac{l^*}{2\pi l_0^*} \right)^2 \right)^{-\mu/2}. \quad (4.1)$$

Following Nikurashin *et al.* (2014), we assume

$$\mu = 3.5, \quad k_0^* = 1.8 \times 10^{-4} \text{ m}^{-1}, \quad l_0^* = 1.8 \times 10^{-4} \text{ m}^{-1}, \quad h^* = 305 \text{ m}. \quad (4.2)$$

After non-dimensionalization, (4.1) reduces to

$$P_\eta = C \left( 1 + \left( \frac{\kappa}{2\pi L^* k_0^*} \right)^2 \right)^{-\mu/2}, \quad C = \frac{\mu - 2}{(2\pi)^3} \left( \frac{h^*}{H_0^* L_0^*} \right)^2. \quad (4.3)$$

The model topography is represented by a sum of Fourier modes with random phases and spectral amplitudes conforming to (4.3). The range of small-scale variability  $L_{min} < 2\pi\kappa^{-1} < L_C$  is specified by assigning  $L_{min} = 0.3$  and  $L_C = 3$ , which is dimensionally equivalent to  $L_{min}^* = 3$  km and  $L_C^* = 30$  km. The components of topography with wavelengths outside of this interval are excluded. The non-dimensional root-mean-square depth variation corresponding to this spectrum is  $\eta_{rms} = 6.14 \times 10^{-2}$ . Simulations are performed using the de-aliased pseudo-spectral model employed in our previous studies (Radko 2021, 2022a) on the computational domain of size  $(L_x, L_y) = (100, 100)$ . All topography-resolving experiments employ a mesh with  $(N_x, N_y) = (4096, 4096)$  grid points. The lateral viscosity is  $\nu = 5 \times 10^{-3}$ , which is equivalent to  $\nu = 50 \text{ m}^2 \text{ s}^{-1}$ , and  $\gamma = \beta = 0$ . These parameters correspond to  $G_{slow} = 8.72 \times 10^{-3}$ ,  $G_{fast} = 1.88 \times 10^{-5}$ , and  $V_C = 4.65 \times 10^{-2}$ .

The following simulations are initiated by the velocity field  $(u_{ini}, v_{ini})$  given by

$$u_{ini} = U_{ini} \tanh(5 \sin(2\pi y L_y^{-1})), \quad v_{ini} = 0, \quad (4.4)$$

which conforms to the periodic boundary conditions of the spectral model. The pattern of  $u_{ini}$  is presented in figure 2(a), and the corresponding streamfunction  $\psi_{ini}$  is shown

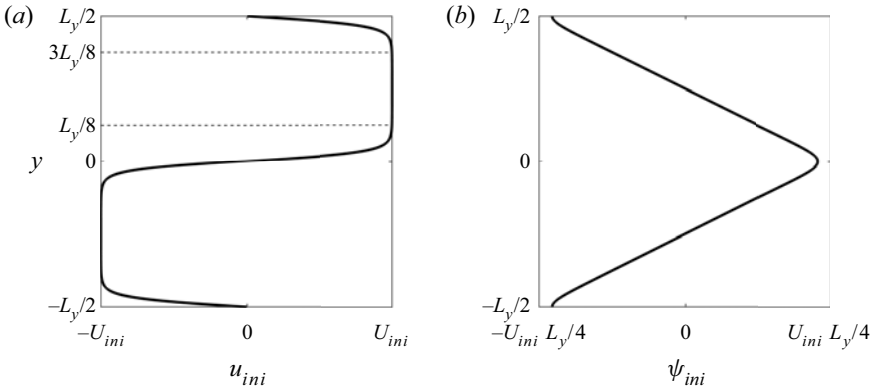


Figure 2. The meridional patterns of the velocity (a) and the streamfunction (b) that are used to initiate topography-resolving simulations. The dashed lines in (a) mark the region  $\Omega$  used for the analysis of the topographic spin-down mechanisms.

in figure 2(b). The pattern represents an almost uniform flow in the region

$$\Omega = \{\frac{1}{8}L_y < y < \frac{3}{8}L_y\}, \tag{4.5}$$

which is meridionally bounded by strong shears. Region  $\Omega$ , marked by dashed lines in figure 2(a), will be used as the testing site for the parameterizations introduced in § 3. Note that the large-scale pattern in figure 2 is symmetric with respect to the  $x$ -axis. Therefore, to avoid redundancy, the following analysis is focused on the northern ( $y > 0$ ) part of the domain.

#### 4.2. Testing the sandpaper theory

The theoretical description (§ 3) greatly simplifies for zonal large-scale flows, leading to

$$\frac{\partial}{\partial t} \frac{\partial^2 \bar{\psi}}{\partial y^2} + D + \nu \frac{\partial^4 \bar{\psi}}{\partial y^4} = 0. \tag{4.6}$$

We neglect the explicit frictional term and integrate (4.6) in  $y$ , which yields

$$\frac{\partial \bar{u}}{\partial t} = -M_x, \tag{4.7}$$

where  $M_x$  is the  $x$ -component of the momentum forcing term defined by (3.16). Our objective is to evaluate fast-flow, slow-flow and hybrid sandpaper models. For zonal currents, these reduce to

$$M_{x \text{ fast}} = \frac{G_{fast}}{\bar{u}}, \quad M_{x \text{ slow}} = G_{slow} \bar{u}, \quad M_{x \text{ hybrid}} = F_C \exp\left(-\sqrt{1 + \ln^2(\bar{u} V_C^{-1})}\right). \tag{4.8}$$

Equation (4.7) offers a convenient opportunity to directly connect simulations and theory since  $\partial \bar{u} / \partial t$  can be easily diagnosed from the topography-resolving simulations, while  $M_x$  can be computed from (4.8). To this end, we perform a series of simulations initiated by (4.4) and performed with various values of  $U_{ini}$ . Each simulation is extended for a period of  $t_0 = 100$ , which is sufficient for the establishment of balanced flows that the sandpaper theory strives to represent. During this interval, the large-scale velocity remains zonal and spatially uniform within the diagnostic area  $\Omega$ . Longer integration periods lead

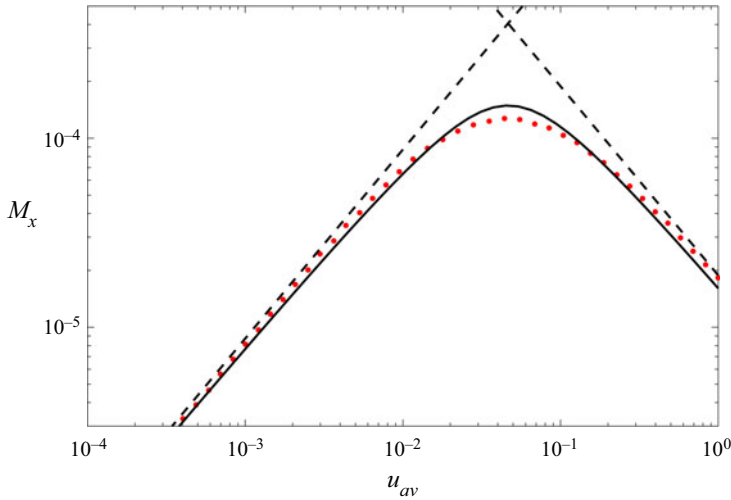


Figure 3. The estimates of the topographic momentum forcing  $M_x$  based on a series of topography-resolving simulations (red dots) are plotted as a function of large-scale velocity on the logarithmic scale. Also shown are the corresponding theoretical predictions based on the slow-flow, fast-flow and hybrid sandpaper models, which are indicated by the dashed line with a positive slope, the dashed line with a negative slope and the solid curve, respectively.

to the development of Kelvin–Helmholtz instabilities, which lead to non-zonal flows, violating the assumptions on which (4.7) and (4.8) are based. The average velocity is evaluated over the second half of the integration interval, which excludes the transient flow-adjustment phase

$$u_{ls} = \langle u \rangle_{x, y \subset \Omega}, \quad u_{av} = \langle u_{ls} \rangle_{0.5t_0 < t < t_0}, \quad (4.9)$$

and  $u_{av}$  is used in theoretical estimates of  $M_x$  based on (4.8). The corresponding numerical values of  $M_x$  are determined from

$$M_x = - \left\langle \frac{\partial u_{ls}}{\partial t} \right\rangle_{0.5t_0 < t < t_0} = \frac{2}{t_0} (u_{ls}|_{t=0.5t_0} - u_{ls}|_{t=t_0}). \quad (4.10)$$

The results (figure 3) reveal the consistency of the proposed closure models and simulations. For relatively low large-scale velocities  $u_{av} < 0.01$ , the numerical estimates of  $M_x$  closely match the slow-flow theory. For  $u_{av} > 0.1$ , simulations approach the fast-flow model. The hybrid model is remarkably accurate throughout the entire range of velocities in figure 3 – values that span more than three orders of magnitude and cover all oceanographically relevant values.

It should be noted that the non-monotonic momentum forcing (figure 3) might have major observable consequences. For instance, this damping pattern could affect the statistics of velocity in the deep ocean, preferentially suppressing flows with speeds close to  $V_C$ . In this regard, it would be desirable to uncover observational evidence of a minimum in the probability distribution function for the abyssal flow speeds that can be unambiguously attributed to the sandpaper effect.

While the foregoing diagnostics (figure 3) have convincingly validated our closure models, it is still interesting to determine how well the sandpaper theory captures the physical mechanisms at play. For that, we first turn to one of the simulations in the fast-flow range. Figure 4 presents the flow pattern realized at  $t = 100$  in the experiment performed with  $U_{ini} = 0.5$ . The key feature of the fast-flow theory is the homogenization of the

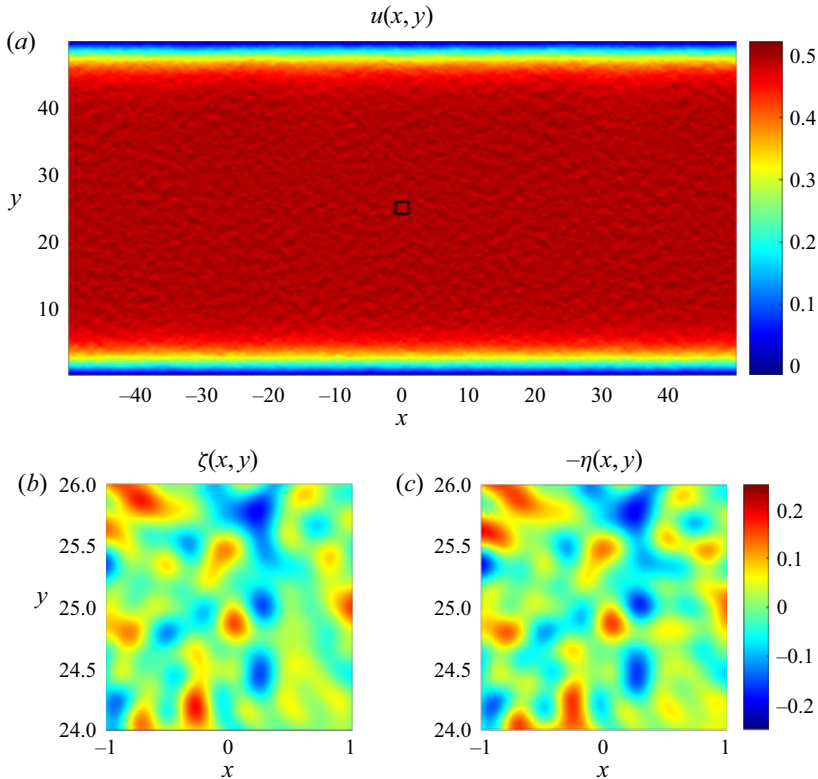


Figure 4. The representative fully developed fast-flow state ( $U_{ini} = 0.5$ ,  $t = 100$ ). Panel (a) shows the zonal velocity in the northern ( $y > 0$ ) part of the computational domain. Panel (b) presents the magnified view of vorticity in the square area marked in (a). The corresponding pattern of  $-\eta$  is shown in (c).

small-scale potential vorticity (3.2). This tendency is spectacularly manifested in patterns of  $\zeta$  (figure 4b) and  $-\eta$  (figure 4c) plotted over a small area marked in figure 4(a) – patterns that are nearly identical in all fine detail.

To offer a more quantitative analysis of the homogenization tendency, we compute the correlation coefficient

$$c_1 = -\frac{\langle \zeta \eta \rangle_{\Omega}}{\sqrt{\langle \zeta^2 \rangle_{\Omega} \langle \eta^2 \rangle_{\Omega}}}. \tag{4.11}$$

For the state shown in figure 4,  $c_1 = 0.9470$ , which supports (3.2). In addition to the instantaneous correlation, we also introduce its temporal average

$$C_1 = \langle c_1 \rangle_{0.5t_0 < t < t_0}. \tag{4.12}$$

The instantaneous correlation coefficients exhibit very limited variation in time in the fully developed flows, and generally  $C_1 \approx c_1$ . For the simulation in figure 4,  $C_1 = 0.9468$ .

For the slow-flow regime, the leading-order balance according to the asymptotic theory (§ 3.2) is between  $A_{ad} = u_{ls}(\partial \eta / \partial x)$  and  $A_{diss} = \nu \nabla^4 \psi$ .  $A_{ad}$  can be physically interpreted as the tendency of water columns to change their rotation rate due to stretching (squeezing) after being advected by the large-scale flow into the deeper (shallower) regions. Term  $A_{diss}$ , on the other hand, represents the frictional spin down. The anticipated balance of  $A_{ad}$  and  $A_{diss}$  is readily confirmed by figure 5, which presents these quantities for one of the slow-flow simulations ( $U_{ini} = 5 \times 10^{-3}$ ). In figure 5,  $A_{ad}$  and  $A_{diss}$  are plotted

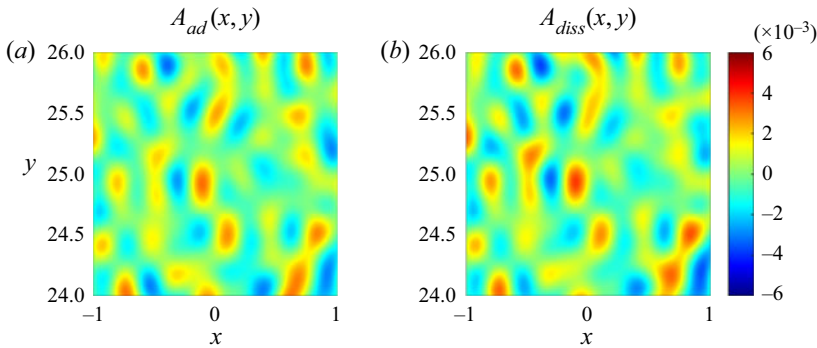


Figure 5. The representative fully developed slow-flow state ( $U_{ini} = 5 \times 10^{-3}$ ,  $t = 100$ ). The advective ( $A_{ad}$ ) and diffusive ( $A_{diss}$ ) components of the expected leading-order balance are shown in (a) and (b), respectively.

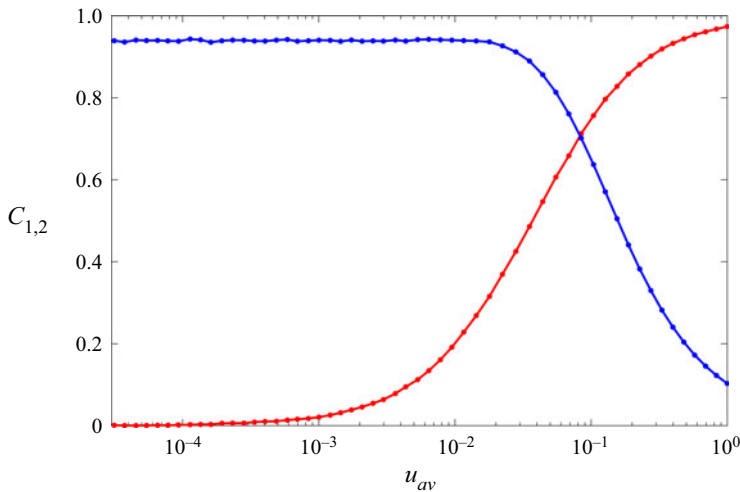


Figure 6. The correlation coefficients  $C_1$  (red curve) and  $C_2$  (blue curve) are plotted as functions of the average flow speed  $u_{av}$ . In relatively swift flows,  $C_1 \approx 1$ , which is consistent with (3.2) and reflects the homogenization of PV. In weak flows,  $C_2 \approx 1$ , which supports the advective-dissipative balance (3.11).

over a small area  $-1 < x < 1$ ,  $24 < y < 26$ , making it possible to visually compare their very similar patterns. For a more quantitative assessment, we introduce the instantaneous correlation coefficient ( $c_2$ ) and its temporal average ( $C_2$ )

$$c_2 = \frac{\langle A_{ad}A_{diss} \rangle_{\Omega}}{\sqrt{\langle A_{ad}^2 \rangle_{\Omega} \langle A_{diss}^2 \rangle_{\Omega}}}, \quad C_2 = \langle c_2 \rangle_{0.5t_0 < t < t_0}. \quad (4.13)$$

For the experiment in figure 5, we obtain  $c_2 = 0.933$  at  $t = 100$  and  $C_2 = 0.941$ .

In figure 6, we consolidate the estimates of time-mean correlation coefficients ( $C_1$ ,  $C_2$ ) from all zonal-flow experiments and plot them as a function of  $u_{av}$ . The results illustrate the transition from the advective-dissipative balance realized at low speeds ( $C_1 \ll 1$ ,  $C_2 \approx 1$ ) to the homogenization of PV for swift currents ( $C_1 \approx 1$ ,  $C_2 \ll 1$ ).

Figures 7 and 8 present an even more stringent test of the hybrid sandpaper model (§ 3.3). Here, we examine the non-zonal flow initiated by

$$u_{ini} = U_{ini} \tanh(5 \sin(2\pi y L_y^{-1})), \quad v_{ini} = 0.1 U_{ini} \sin(2\pi x L_x^{-1}), \quad (4.14)$$

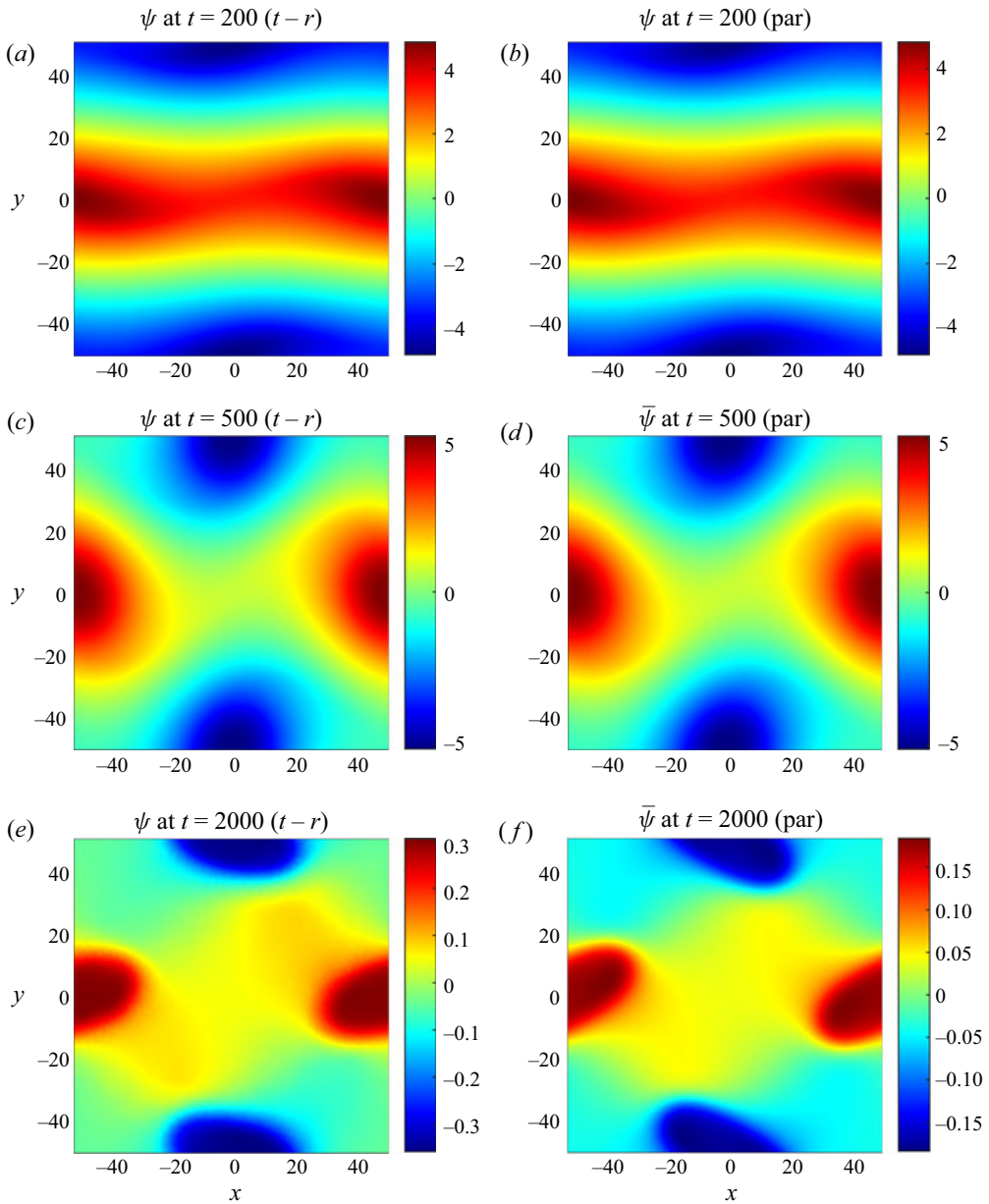


Figure 7. The snapshots of the streamfunction at  $t = 200, 500$  and  $2000$  in the topography-resolving  $(a,c,e)$  and parametric  $(b,d,f)$  simulations.

and compare the topography-resolving simulation with the corresponding parametric solution based on (3.26). In the following experiments, we use  $U_{ini} = 0.2$ , which places the initial current in the category of fast flows. However, as the simulations are extended in time and velocities throughout the domain gradually reduce, these systems transition first into the intermediate-flow and, subsequently, the slow-flow regime. Thus, the analysis of the entire evolutionary pattern makes it possible to assess the performance of the hybrid sandpaper model in all three dynamically dissimilar regimes.



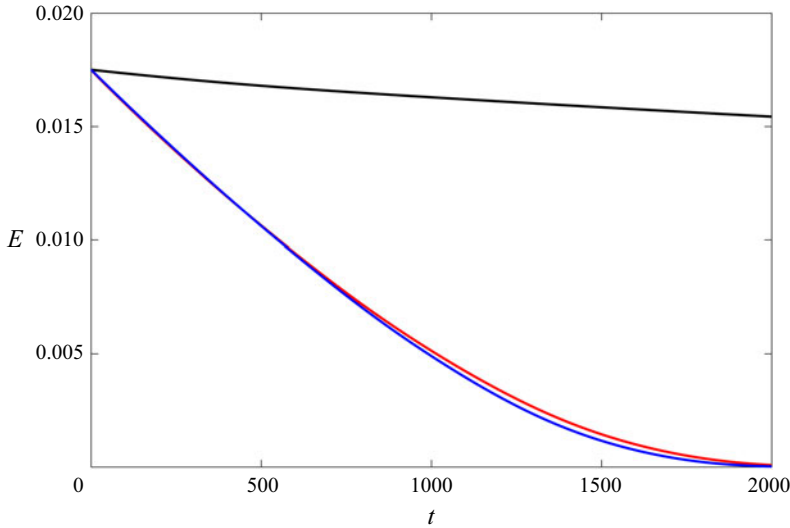


Figure 8. The time series of mean kinetic energy. The topography-resolving, parametric and flat-bottom simulations are indicated by red, blue and black curves, respectively.

Since the parametric simulation does not require resolving rough topography and the associated small-scale flow features, it was performed on a relatively coarse grid with  $(N_x, N_y) = (256, 256)$ . Both simulations, topography resolving and parametric, were extended for 2000 time units. The results leave no doubt about the efficacy of the sandpaper theory. The flow fields in these simulations (figure 7) closely follow each other for most of the integration interval. Only in their final stages ( $t > 1000$ ) do these solutions visibly diverge. The temporal records of the kinetic energy (figure 8) further reinforce and quantify this conclusion. Until  $t = 1000$ , which is dimensionally equivalent to  $t^* \approx 100$  days, the relative differences in the kinetic energy does not exceed 5%. We also emphasize the dramatic dissimilarity in the evolution of the corresponding flat-bottom simulation, also shown in figure 8. During these experiments, the kinetic energy in the topography-resolving and parametric simulations plunged by more than two orders of magnitude. In the flat-bottom run, it reduced by merely 12%.

#### 4.3. Other evolutionary patterns

A series of simulations exemplified by the experiments in §4.2 indicate that the slow-hybrid-fast framework adequately describes the evolution of large-scale flows for the oceanographically relevant range of submesoscale eddy viscosities  $1 \text{ m}^2 \text{ s}^{-1} \lesssim \nu^* \lesssim 100 \text{ m}^2 \text{ s}^{-1}$  (e.g. Li, Sun, & Xu 2018). The defining feature of these systems is relatively low values of the effective Taylor numbers  $Ta \equiv f_0^{*2} L^{*4} / \nu^{*2} \lesssim O(10^6)$ . However, some reflection suggests that expanding the analysis beyond this strongly dissipative regime is bound to reveal a fundamentally different dynamics.

In particular, we note that a large-scale current can transition into a PV-homogenized state satisfying (3.2) only if it is relatively swift to begin with:  $U \gtrsim \eta$ . This implies that the fast-flow model (§4.1) cannot in principle represent the regime in which

$$U^* \ll \frac{\eta^* f_0^* L^*}{H_0^*}. \quad (4.15)$$

Likewise, the advective-dissipative balance  $u_{1s}(\partial\eta/\partial x) \approx v\nabla^4\psi$  – the cornerstone of the slow-flow theory – is unlikely to be realized in systems with weak friction

$$v^* \ll \frac{\eta^* f_0^* L^{*2}}{H_0^*}. \tag{4.16}$$

Thus, the present version of the sandpaper theory (§3) does not capture systems with parameters concurrently satisfying both (4.15) and (4.16).

To bring some insight into the dynamics of such flows, we perform a series of simulations analogous to those in figure 4 in which  $Ro$  is systematically decreased and  $Re$  is increased. These experiments reveal two well-defined evolutionary patterns, the Taylor-column and the topographic Rossby wave regime, and various outcomes that are less clear cut. The Taylor-column regime tends to be realized for  $10^{-4} < U_{ini} < 10^{-3}$  and  $Ta \gtrsim 10^{20}$ . In this scenario, the initially uniform flow gradually reorganizes into recirculating patterns with fluid trapped in their interior. A representative experiment is shown in figure 9(a). Here we present a magnified view of the streamfunction over a small area  $-1 < x < 1$ ,  $24 < y < 26$ , superimposed on the contours of the topography. These diagnostics reveal the alignment of the flow along the isobaths in a spectacular manifestation of the topographic steering effect. The eddies in figure 9(a) are quasi-steady and centred directly above the underwater hills and valleys. However, when the initial velocity is further reduced to  $U_{ini} < 10^{-4}$ , the Taylor-column regime gives way to the continuously oscillating pattern that we interpret as a disorganized field of topographic Rossby waves (figure 9b). In contrast to the Taylor-column regime, strong perturbations in figure 9(b) are mostly concentrated on the topographic slopes. Large-scale flows in the Taylor-column and topographic-wave regimes are characterized by comparable spin-down rates. While of limited relevance to the ocean, slow non-dissipative systems exemplified by the states in figure 9 are of interest in their own right and should be explored further for completeness.

### 5. The multilayer model

The governing equations for the multilayer quasi-geostrophic rigid-lid model (e.g. Pedlosky 1987) are

$$\left\{ \begin{array}{l} \frac{\partial q_1^*}{\partial t^*} + J(\psi_1^*, q_1^*) + \beta^* \frac{\partial \psi_1^*}{\partial x^*} = v^* \nabla^4 \psi_1^*, \quad q_1^* = \nabla^2 \psi_1^* + \frac{f_0^{*2}}{g^* H_1^*} (\psi_2^* - \psi_1^*), \\ \frac{\partial q_i^*}{\partial t^*} + J(\psi_i^*, q_i^*) + \beta^* \frac{\partial \psi_i^*}{\partial x^*} = v^* \nabla^4 \psi_i^*, \quad q_i^* = \nabla^2 \psi_i^* + \frac{f_0^{*2}}{g^* H_i^*} (\psi_{i-1}^* + \psi_{i+1}^* - 2\psi_i^*), \\ \quad i = 2, \dots, (n-1) \\ \frac{\partial q_n^*}{\partial t^*} + J(\psi_n^*, q_n^*) + \beta^* \frac{\partial \psi_n^*}{\partial x^*} \\ \quad = v^* \nabla^4 \psi_n^* - \gamma^* \nabla^2 \psi_n^*, \quad q_n^* = \nabla^2 \psi_n^* + \frac{f_0^{*2}}{g^* H_n^*} (\psi_{n-1}^* - \psi_n^*) + f_0^* \frac{\eta^*}{H_n^*}, \end{array} \right. \tag{5.1}$$

where  $\psi_i^*$  is the streamfunction in layer  $i$  and  $H_i^*$  is the reference layer thickness. The reduced gravity is denoted by  $g^* = g^*(\Delta\rho^*/\rho_0^*)$ , where  $g^* \approx 9.8 \text{ m s}^{-2}$  is the standard gravity, and  $\rho_0^*$  is the reference density. We assume identical density differences between adjacent layers  $\Delta\rho^* = \rho_i^* - \rho_{i-1}^*$ , although the generalization to variable  $\Delta\rho^*$  is straightforward.

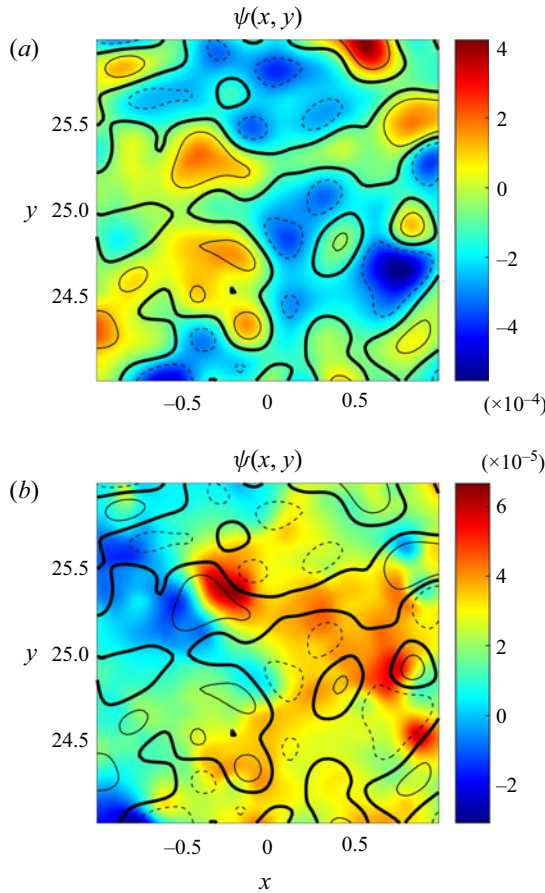


Figure 9. Representative flow patterns in the Taylor-column (a) and topographic-wave (b) regimes. The initial velocity of  $U_{ini} = 2 \times 10^{-3}$  was used in (a), whereas the simulation in (b) was performed with  $U_{ini} = 2 \times 10^{-4}$ . In both cases,  $\nu = 10^{-6}$  and  $t = 1000$ . The isobaths with  $\eta = -0.07, 0$  and  $0.07$  are indicated by the dashed, heavy solid and light solid curves, respectively.

The non-dimensionalization of (5.1) is based on (2.3), and the lowest layer depth  $H_n^*$  is used as a unit of topographic height

$$\eta^* = H_n^* \eta. \tag{5.2}$$

In non-dimensional units, system (5.1) reduces to

$$\begin{cases} \frac{\partial q_1}{\partial t} + J(\psi_1, q_1) + \beta \frac{\partial \psi_1}{\partial x} = \nu \nabla^4 \psi_1, & q_1 = \nabla^2 \psi_1 + F_1(\psi_2 - \psi_1), \\ \frac{\partial q_i}{\partial t} + J(\psi_i, q_i) + \beta \frac{\partial \psi_i}{\partial x} = \nu \nabla^4 \psi_i, & q_i = \nabla^2 \psi_i + F_i(\psi_{i-1} + \psi_{i+1} - 2\psi_i), \\ i = 2, \dots, (n-1) \\ \frac{\partial q_n}{\partial t} + J(\psi_n, q_n) + \beta \frac{\partial \psi_n}{\partial x} \\ = \nu \nabla^4 \psi_n - \gamma \nabla^2 \psi_n, & q_n = \nabla^2 \psi_n + F_n(\psi_{n-1} - \psi_n) + \eta, \end{cases} \tag{5.3}$$

where  $F_i = f_0^2 L^2 / g' H_i$  is the inverse Burger number.

The fast-flow limit (3.1) was considered by Radko (2022b), resulting in

$$\left\{ \begin{array}{l} \frac{\partial \bar{q}_1}{\partial t} + J(\bar{\psi}_1, \bar{q}_1) + \beta \frac{\partial \bar{\psi}_1}{\partial x} = \nu \nabla^4 \bar{\psi}_1, \quad \bar{q}_1 = \nabla^2 \bar{\psi}_1 + F_1(\bar{\psi}_2 - \bar{\psi}_1), \\ \frac{\partial \bar{q}_i}{\partial t} + J(\bar{\psi}_i, \bar{q}_i) + \beta \frac{\partial \bar{\psi}_i}{\partial x} = \nu \nabla^4 \bar{\psi}_i, \quad \bar{q}_i = \nabla^2 \bar{\psi}_i + F_i(\bar{\psi}_{i-1} + \bar{\psi}_{i+1} - 2\bar{\psi}_i), \\ i = 2, \dots, (n-1), \\ \frac{\partial \bar{q}_n}{\partial t} + J(\bar{\psi}_n, \bar{q}_n) + \beta \frac{\partial \bar{\psi}_n}{\partial x} + D_{fast} \quad \bar{q}_n = \nabla^2 \bar{\psi}_n + F_n(\bar{\psi}_{n-1} - \bar{\psi}_n) + \eta_L. \\ = \nu \nabla^4 \bar{\psi}_n - \gamma \nabla^2 \bar{\psi}_n, \end{array} \right. \quad (5.4)$$

The topographic forcing term ( $D_{fast}$ ) appears only in the bottom layer equation, and it takes the form of

$$D_{fast} = G_{fast} \left( \frac{\partial}{\partial x} \left( \frac{v_n}{u_n^2 + v_n^2} \right) - \frac{\partial}{\partial y} \left( \frac{u_n}{u_n^2 + v_n^2} \right) \right), \quad G_{fast} = 2\pi \int |\tilde{\eta}_S|^2 \left( \frac{\gamma}{\kappa} + \nu \kappa \right) d\kappa, \quad (5.5)$$

where  $(u_n, v_n) = (-\partial \psi_n / \partial y, \partial \psi_n / \partial x)$ .

The theory development for slow-flow limit (3.6) parallels its barotropic counterpart (§ 3.2) and is presented in the abbreviated form. We adopt the scaling system in (3.6) and (3.9), and rescale  $F_i$  as

$$F_i = \varepsilon^2 F_i^{(0)}. \quad (5.6)$$

The solution in each layer  $i$  is then sought in terms of power series

$$\psi_i = \varepsilon \psi_i^{(1)}(X, Y, T) + \varepsilon^3 \psi_i^{(3)}(X, Y, x, y, T) + O(\varepsilon^4). \quad (5.7)$$

The leading-order  $O(\varepsilon^4)$  balance in all layers except for the lowest one is trivially satisfied by

$$\psi_i^{(3)} = 0, \quad i = 1, \dots, (n-1), \quad (5.8)$$

whereas for the bottom layer, it takes the form

$$\frac{\partial \psi_n^{(1)}}{\partial X} \frac{\partial \eta_{S0}}{\partial y} - \frac{\partial \psi_n^{(1)}}{\partial Y} \frac{\partial \eta_{S0}}{\partial x} = \nu_0 \nabla^4 \psi_n^{(3)}. \quad (5.9)$$

The evolutionary large-scale equations are obtained by averaging the  $O(\varepsilon^6)$  balances in  $(x, y)$ . The resulting expressions are then rewritten in terms of the original variables,

leading to

$$\left\{ \begin{array}{l} \frac{\partial \bar{q}_1}{\partial t} + J(\bar{\psi}_1, \bar{q}_1) + \beta \frac{\partial \bar{\psi}_1}{\partial x} = \nu \nabla^4 \bar{\psi}_1, \quad \bar{q}_1 = \nabla^2 \bar{\psi}_1 + F_1(\bar{\psi}_2 - \bar{\psi}_1), \\ \frac{\partial \bar{q}_i}{\partial t} + J(\bar{\psi}_i, \bar{q}_i) + \beta \frac{\partial \bar{\psi}_i}{\partial x} = \nu \nabla^4 \bar{\psi}_i, \quad \bar{q}_i = \nabla^2 \bar{\psi}_i + F_i(\bar{\psi}_{i-1} + \bar{\psi}_{i+1} - 2\bar{\psi}_i), \\ \quad i = 2, \dots, (n-1) \\ \frac{\partial \bar{q}_n}{\partial t} + J(\bar{\psi}_n, \bar{q}_n) + \beta \frac{\partial \bar{\psi}_n}{\partial x} + D_{slow} \\ = \nu \nabla^4 \bar{\psi}_n - \gamma \nabla^2 \bar{\psi}_n, \quad \bar{q}_n = \nabla^2 \bar{\psi}_n + F_n(\bar{\psi}_{n-1} - \bar{\psi}_n) + \eta_L, \end{array} \right. \quad (5.10)$$

where  $\bar{\psi}_i = \varepsilon \psi_i^{(1)}$ , and

$$D_{slow} = G_{slow} \left( \frac{\partial \bar{v}_n}{\partial x} - \frac{\partial \bar{u}_n}{\partial y} \right), \quad G_{slow} = \pi \int \frac{|\tilde{\eta}_S|^2}{\nu \kappa} d\kappa. \quad (5.11)$$

Systems (5.4) and (5.10) represent the limits of slow and fast flows. A challenge that naturally arises at this point is the development of a universal framework that would apply to a wide range of velocities. We also insist that such a framework must be fully consistent with (5.4) and (5.10) in the limits of high and low velocities, respectively. Fortunately, the structural similarity of the topographic forcing terms (5.5) and (5.11) to their homogeneous counterparts (§ 3) makes it possible to adopt the previously developed and tested hybrid model (3.25) with only minimal modifications

$$D_{hybrid} = \frac{\partial}{\partial x} \left[ \bar{v}_n \bar{V}_n^{-1} F_C \exp \left\{ -\sqrt{1 + \ln^2(\bar{V}_n V_C^{-1})} \right\} \right] - \frac{\partial}{\partial y} \left[ \bar{u}_n \bar{V}_n^{-1} F_C \exp \left\{ -\sqrt{1 + \ln^2(\bar{V}_n V_C^{-1})} \right\} \right], \quad (5.12)$$

where  $\bar{V}_n = \sqrt{\bar{u}_n^2 + \bar{v}_n^2}$ . Replacing  $D_{fast}$  and  $D_{slow}$  in (5.4) and (5.10) by the hybrid expression (5.12) completes the development of a general theory of flow forcing by rough topography – the main objective of our study.

To simplify the implementation of the proposed theory in future investigations, we also include the dimensional expression of the topographic forcing

$$D_{hybrid}^* = \frac{\partial}{\partial x^*} \left[ \frac{\bar{v}_n^*}{\bar{V}_n^*} F_C^* \exp \left\{ -\sqrt{1 + \ln^2 \left( \frac{\bar{V}_n^*}{V_C^*} \right)} \right\} \right] - \frac{\partial}{\partial y^*} \left[ \frac{\bar{u}_n^*}{\bar{V}_n^*} F_C^* \exp \left\{ -\sqrt{1 + \ln^2 \left( \frac{\bar{V}_n^*}{V_C^*} \right)} \right\} \right], \quad (5.13)$$

where  $\bar{V}_n^* = \sqrt{\bar{u}_n^{*2} + \bar{v}_n^{*2}}$ ,  $V_C^* = \sqrt{G_{fast}^*/G_{slow}^*}$ ,  $F_C^* = \sqrt{G_{fast}^* G_{slow}^*}$  and

$$G_{fast}^* = \frac{2\pi f_0^{*2}}{H_n^{*2}} \int |\tilde{\eta}_S^*|^2 \left( \frac{\gamma^*}{\kappa^*} + \nu^* \kappa^* \right) d\kappa^*, \quad G_{slow}^* = \frac{\pi \nu_0^{*2}}{H_n^{*2}} \int \frac{|\tilde{\eta}_S^*|^2}{\nu^* \kappa^*} d\kappa^*. \quad (5.14)$$

Term (5.13) can be introduced in the bottom layer equation in (5.1) to represent the effects of unresolved bathymetry. We also note that adding  $D_{hybrid}^*$  to the potential vorticity

equation is equivalent to modifying the horizontal momentum equations as follows:

$$\begin{cases} \frac{\partial u_n^*}{\partial t^*} + u_n^* \frac{\partial u_n^*}{\partial x^*} + v_n^* \frac{\partial u_n^*}{\partial y^*} - f^* v_n^* = -\frac{1}{\rho_n^*} \frac{\partial p_n^*}{\partial x^*} - M_x^* + \nu^* \nabla^2 u_n^*, \\ \frac{\partial v_n^*}{\partial t^*} + u_n^* \frac{\partial v_n^*}{\partial x^*} + v_n^* \frac{\partial v_n^*}{\partial y^*} + f^* u_n^* = -\frac{1}{\rho_n^*} \frac{\partial p_n^*}{\partial y^*} - M_y^* + \nu^* \nabla^2 v_n^*, \end{cases} \quad (5.15)$$

where  $p_n^*$  is the pressure field in the bottom layer, and

$$\begin{cases} M_x^* = \frac{\bar{u}_n^*}{\bar{V}_n^*} F_C^* \exp \left\{ -\sqrt{1 + \ln^2 \left( \frac{\bar{V}_n^*}{\bar{V}_C^*} \right)} \right\}, \\ M_y^* = \frac{\bar{v}_n^*}{\bar{V}_n^*} F_C^* \exp \left\{ -\sqrt{1 + \ln^2 \left( \frac{\bar{V}_n^*}{\bar{V}_C^*} \right)} \right\}. \end{cases} \quad (5.16)$$

Formulation (5.16) makes it possible to implement the hybrid parameterization of rough topography in multilayer general circulation models (e.g. Bleck 2002).

## 6. Discussion

At the time of this writing, it is generally accepted that rough topography can strongly influence the intensity and variability of large-scale and mesoscale flows in the ocean (e.g. LaCasce *et al.* 2019; Radko 2020; Gulliver & Radko 2022). However, our understanding of the specific mechanisms of bathymetric control and our ability to concisely represent it in theoretical and coarse-resolution numerical models remain limited. Our recent efforts (Radko 2022a,b) have led to the development of the analytical ‘sandpaper’ model that captures the effects of irregular topographic features, provided that the spectrum of sea-floor depth is known. The model of Radko (2022a,b) performed well for relatively fast flows but exhibited unphysical behaviour in the low-speed limit. This complication motivates the present attempt to formulate the second-generation sandpaper model that is uniformly valid for all oceanographically relevant velocity values.

To this end, we have explored two fundamentally different regimes, represented by the asymptotic limits of low and high flow speeds. Both limits were treated using conventional multiscale methods (e.g. Mei & Vernescu 2010), leading to the analytical description of large-scale forcing by rough bathymetry. We also took advantage of the dynamical transparency of multiscale theories, which made it possible to unambiguously identify the essential physical mechanisms at play. In the fast-flow regime, the key phenomenon is the homogenization of potential vorticity. Homogenization controls the dynamics of small-scale topographically generated eddies and the associated Reynolds stresses. Surprisingly, the eddy stresses dominate the net topographic forcing of swift large-scale flows, whereas the form drag, which is invoked in flow-topography interaction theories more often, turned out to be largely inconsequential. However, the situation changes cardinally for slow currents. In this regime, the small-scale dynamics is governed by the balance between the torque associated with the stretching/squeezing of water columns and their frictional spin down. The topographic form drag becomes the primary large-scale forcing mechanism, while the Reynolds stresses are weak and dynamically insignificant. These mechanisms control the flow-topography interaction in both homogeneous (§ 3) and layered (§ 5) models.

From a pragmatic perspective, the key advancement brought by this study is a generic hybrid model that encompasses both slow-flow and fast-flow limits. In essence, this

model represents a rigorous asymptotics-based parameterization of the effects of rough topography. It naturally lends itself to the implementation in layered oceanic general circulation models, which are commonly used in climate prediction studies and for operational forecasting. Despite continuous progress in high-performance computing, roughness-resolving models will not be used for extended global simulations in the foreseeable future. The sandpaper model, on the other hand, is expected to improve the accuracy of simulations without the major increase in resolution and associated computational costs.

The explicit nature of the sandpaper model also opens a pathway for in-depth theoretical analyses of the myriad processes that are affected by the bottom roughness. Future studies should address the impact of irregular topography on subtropical and subpolar gyres, the Antarctic Circumpolar Current, large-scale waves, baroclinic and barotropic instabilities and boundary currents – among many other oceanic systems. The existing evidence indicates that the impact of bottom roughness is profound, and the sandpaper theory can make such problems ultimately tractable.

On a more technical side, it would be highly desirable to transition from the quasi-geostrophic framework to more general systems, including the shallow-water and, eventually, full Navier–Stokes equations. The quasi-geostrophic approximation is assumed here to minimize complexity and enhance dynamic transparency. However, the flow speed at some locations in the ocean can exceed its formal applicability limits. Therefore, new versions of the sandpaper theory should be capable of representing strongly nonlinear systems with order-one Rossby numbers. Recent progress in this direction has been encouraging. Gulliver & Radko (2023) abandoned the quasi-geostrophic approximation and performed a series of simulations of flows over rough topography with the barotropic Navier–Stokes model. The key features of these experiments – including the PV-homogenization and the inverse velocity-drag relation – proved to be consistent with the sandpaper theory.

**Acknowledgements.** The author thanks N. Balmforth and the anonymous reviewers for helpful comments.

**Funding.** Support of the National Science Foundation (grant OCE 1828843) is gratefully acknowledged.

**Declaration of interests.** The author reports no conflict of interest.

**Author ORCIDs.**

 Timour Radko <https://orcid.org/0000-0002-5682-280X>.

## Appendix A. Auxiliary steps in the development of the asymptotic slow-flow model

The objective of the following analysis is the explicit expression of the topographic forcing function (3.13) in terms of the properties of the large-scale flow. The calculations are conveniently performed in the flow-following small-scale coordinate system:

$$\begin{cases} x' = x \cos \theta + y \sin \theta, \\ y' = -x \sin \theta + y \cos \theta. \end{cases} \quad (\text{A1})$$

The flow-orientation variable  $\theta$  in (A1) is defined by

$$\cos(\theta) = -\frac{1}{V} \frac{\partial \psi^{(1)}}{\partial Y}, \quad \sin(\theta) = \frac{1}{V} \frac{\partial \psi^{(1)}}{\partial X}, \quad (\text{A2})$$

where  $V = \sqrt{(\partial\psi^{(1)}/\partial Y)^2 + (\partial\psi^{(1)}/\partial X)^2}$ . In the new coordinate system, (3.11) takes the form

$$V \frac{\partial \eta_{S0}}{\partial x'} = \nu_0 \nabla^4 \psi^{(3)} \tag{A3}$$

and (3.13) is written as

$$D_{slow\ 0} = \frac{\partial}{\partial X} (D_V \sin \theta + D_U \cos \theta) - \frac{\partial}{\partial Y} (D_V \cos \theta - D_U \sin \theta), \tag{A4}$$

where

$$D_V = \left\langle \psi^{(3)} \frac{\partial \eta_{S0}}{\partial x'} \right\rangle_{x',y'}, \quad D_U = \left\langle \psi^{(3)} \frac{\partial \eta_{S0}}{\partial y'} \right\rangle_{x',y'}. \tag{A5}$$

The  $D_U$  term can be shown to be inconsequential based on its symmetries. Reversing the  $x'$ -orientation of small-scale bathymetry  $\eta_S \rightarrow \eta_S(-x', y')$  reverses the sign of  $\psi^{(3)} \rightarrow -\psi^{(3)}(-x', y')$ , which, in turn, reverses the sign of  $D_U$ . Thus, any statistical averaging that assigns equal weights to a given pattern of  $\eta_S$  and its mirror image results in the net cancellation of their contributions to  $D_U$ .

To obtain an explicit expression for  $D_V$ , we eliminate  $\partial \eta_{S0}/\partial x'$  in (A5) using (A3), which yields

$$D_V = V^{-1} \langle \psi^{(3)} \nu_0 \nabla^4 \psi^{(3)} \rangle_{x',y'}. \tag{A6}$$

This expression is further simplified using the Parseval identity

$$D_V = V^{-1} \iint \tilde{\psi}^{(3)} \cdot \text{conj}(\nu_0 \kappa^4 \tilde{\psi}^{(3)}) \, dk' \, dl', \tag{A7}$$

where  $(k', l')$  are the small-scale wavenumbers in the flow-following coordinate system and  $\kappa^2 = k'^2 + l'^2$ . To evaluate the double integral in (A7), we use polar coordinates defined as

$$k' = \kappa \cos \varphi, \quad l' = \kappa \sin \varphi, \tag{A8}$$

which further reduces (A7) to

$$D_V = V^{-1} \iint |\tilde{\psi}^{(3)}(\kappa, \varphi)|^2 \nu_0 \kappa^4 \kappa \, d\kappa \, d\varphi. \tag{A9}$$

Next,  $D_V$  is expressed in terms of the spectrum of small-scale topography. This is accomplished by applying the Fourier transform to (A3) and evaluating the squared absolute values of both sides of the resulting equation

$$V^2 \kappa^2 \cos^2 \varphi |\tilde{\eta}_{S0}|^2 = (\nu_0 \kappa^4)^2 |\tilde{\psi}^{(3)}|^2. \tag{A10}$$

In this study, we consider statistically isotropic spectra of topography, with  $|\tilde{\eta}_{S0}|^2$  fully determined by  $\kappa$ . For such patterns, we can conveniently link topography and



streamfunction by integrating (A10) in  $\varphi$

$$\pi V^2 \kappa^2 |\tilde{\eta}_{S0}|^2 = (\nu_0 \kappa^4)^2 \int |\tilde{\psi}^{(3)}|^2 d\varphi, \quad (\text{A11})$$

which reduces (A9) to

$$D_V = \pi V \int \frac{\kappa |\tilde{\eta}_{S0}|^2}{\nu_0 \kappa^2} d\kappa. \quad (\text{A12})$$

Finally, we compute (A4):

$$D_{slow\ 0} = G_{slow\ 0} \left( \frac{\partial^2 \psi^{(1)}}{\partial X^2} + \frac{\partial^2 \psi^{(1)}}{\partial Y^2} \right), \quad (\text{A13})$$

where

$$G_{slow\ 0} = \pi \int \frac{|\tilde{\eta}_{S0}|^2}{\nu_0 \kappa} d\kappa. \quad (\text{A14})$$

#### REFERENCES

- BALMFORTH, N.J. & YOUNG, Y.-N. 2002 Stratified Kolmogorov flow. *J. Fluid Mech.* **450**, 131–167.
- BALMFORTH, N.J. & YOUNG, Y.-N. 2005 Stratified Kolmogorov flow. Part 2. *J. Fluid Mech.* **528**, 23–42.
- BENILOV, E.S. 2000 The stability of zonal jets in a rough-bottomed ocean on the barotropic beta plane. *J. Phys. Oceanogr.* **30**, 733–740.
- BENILOV, E.S. 2001 Baroclinic instability of two-layer flows over one-dimensional bottom topography. *J. Phys. Oceanogr.* **31**, 2019–2025.
- BLECK, R. 2002 An oceanic general circulation model framed in hybrid isopycnic–Cartesian coordinates. *Ocean Model.* **4**, 55–58.
- DEWAR, W.K., BERLOFF, P. & HOGG, A.M. 2011 Submesoscale generation by boundaries. *J. Mar. Res.* **69**, 501–522.
- DEWAR, W.K. & HOGG, A.M. 2010 Topographic inviscid dissipation of balanced flow. *Ocean Model.* **32**, 1–13.
- EDEN, C., OLBERS, D. & ERIKSEN, T. 2021 A closure for lee wave drag on the large-scale ocean circulation. *J. Phys. Oceanogr.* **51**, 3573–3588.
- GAMA, S., VERGASSOLA, M. & FRISCH, U. 1994 Negative eddy viscosity in isotropically forced 2-dimensional flow – linear and nonlinear dynamics. *J. Fluid Mech.* **260**, 95–126.
- GOFF, J.A. & JORDAN, T.H. 1988 Stochastic modeling of seafloor morphology: inversion of sea beam data for second-order statistics. *J. Geophys. Res.* **93**, 13589–13608.
- GOLDSMITH, E.J. & ESLER, J.G. 2021 Wave propagation in rotating shallow water in the presence of small-scale topography. *J. Fluid Mech.* **923**, A24.
- GULLIVER, L. & RADKO, T. 2022 topographic stabilization of ocean rings. *Geophys. Res. Lett.* **49**, e2021GL097686.
- GULLIVER, L.T. & RADKO, T. 2023 Virtual laboratory experiments on the interaction of a vortex with small-scale topography. *Phys. Fluids* **35**, 021703.
- HOLLOWAY, G. 1987 Systematic forcing of large-scale geophysical flows by eddy-topography interaction. *J. Fluid Mech.* **184**, 463–476.
- HOLLOWAY, G. 1992 Representing topographic stress for large-scale ocean models. *J. Phys. Oceanogr.* **22**, 1033–1046.
- HUGHES, C.W. & DE CUEVAS, B.A. 2001 Why western boundary currents in realistic oceans are inviscid: a link between form stress and bottom pressure torques. *J. Phys. Oceanogr.* **31**, 2871–2885.
- JACKSON, L., HUGHES, C.W. & WILLIAMS, R.G. 2006 Topographic control of basin and channel flows: the role of bottom pressure torques and friction. *J. Phys. Oceanogr.* **36**, 1786–1805.
- JOHNSON, E.R. 1978 Trapped vortices in rotating flow. *J. Fluid Mech.* **86**, 209–224.
- KLYMAK, J.M., BALWADA, D., GARABATO, A.N. & ABERNATHEY, R. 2021 Parameterizing nonpropagating form drag over rough bathymetry. *J. Phys. Oceanogr.* **51**, 1489–1501.
- LACASCE, J., ESCARTIN, J., CHASSIGNET, E.P. & XU, X. 2019 Jet instability over smooth, corrugated, and realistic bathymetry. *J. Phys. Oceanogr.* **49**, 585–605.

- LI, Q.Y., SUN, L. & XU, C. 2018 The lateral eddy viscosity derived from the decay of oceanic mesoscale eddies. *Open J. Mar. Sci.* **8**, 152–172.
- MANFROI, A. & YOUNG, W. 1999 Slow evolution of zonal jets on the beta plane. *J. Atmos. Sci.* **56**, 784–800.
- MANFROI, A. & YOUNG, W. 2002 Stability of beta-plane Kolmogorov flow. *Physica D* **162**, 208–232.
- MARSHALL, D. 1995 Topographic steering of the antarctic circumpolar current. *J. Phys. Oceanogr.* **25**, 1636–1650.
- MEI, C.C. & VERNESCU, M. 2010 *Homogenization Methods for Multiscale Mechanics*. World Scientific Publishing, London.
- MERRYFIELD, W.J. 2005 Ocean mixing in 10 steps. *Science* **308**, 641–642.
- MESHALKIN, L. & SINAI, Y. 1961 Investigation of the stability of a stationary solution of a system of equations for the plane movement of an incompressible viscous fluid. *J. Appl. Math. Mech.* **25**, 1700–1705.
- NAVEIRA GARABATO, A.C., NÜRSEER, A.G., SCOTT, R.B. & GOFF, J.A. 2013 The impact of small-scale topography on the dynamical balance of the ocean. *J. Phys. Oceanogr.* **43**, 647–668.
- NIKURASHIN, M., FERRARI, R., GRISOUARD, N. & POLZIN, K. 2014 The impact of finite-amplitude bottom topography on internal wave generation in the Southern Ocean. *J. Phys. Oceanogr.* **44**, 2938–2950.
- NOVIKOV, A. & PAPANICOLAOU, G. 2001 Eddy viscosity of cellular flows. *J. Fluid Mech.* **446**, 173–198.
- PARSEVAL, M.-A. 1806 Mémoire sur les séries et sur l'intégration complète d'une équation aux différences partielles linéaires du second ordre, à coefficients constants. Mém. prés. par divers savants. *Acad. des Sciences, Paris* **1**, 638–648.
- PEDLOSKY, J. 1987 *Geophysical Fluid Dynamics*. Springer.
- RADKO, T. 2011a On the generation of large-scale structures in a homogeneous eddy field. *J. Fluid Mech.* **668**, 76–99.
- RADKO, T. 2011b Eddy viscosity and diffusivity in the modon-sea model. *J. Mar. Res.* **69**, 723–752.
- RADKO, T. 2020 Control of baroclinic instability by submesoscale topography. *J. Fluid Mech.* **882**, A14.
- RADKO, T. 2021 Barotropic instability of a time-dependent parallel flow. *J. Fluid Mech.* **922**, A11.
- RADKO, T. 2022a Spin-down of a barotropic vortex by irregular small-scale topography. *J. Fluid Mech.* **944**, A5.
- RADKO, T. 2022b Spin-down of a baroclinic vortex by irregular small-scale topography. *J. Fluid Mech.* **953**, A7.
- RADKO, T. & KAMENKOVICH, I. 2017 On the topographic modulation of large-scale eddying flows. *J. Phys. Oceanogr.* **47**, 2157–2172.
- STEWART, A.L., MCWILLIAMS, J.C. & SOLODOCH, A. 2021 On the role of bottom pressure torques in wind-driven gyres. *J. Phys. Oceanogr.* **51**, 1441–1464.
- TAYLOR, G.I. 1923 Experiments on the motion of solid bodies in rotating fluids. *Proc. Roy. Soc. A* **104**, 213–218.
- VANNESTE, J. 2000 Enhanced dissipation for quasi-geostrophic motion over small-scale topography. *J. Fluid Mech.* **407**, 105–122.
- VANNESTE, J. 2003 Nonlinear dynamics over rough topography: homogeneous and stratified quasi-geostrophic theory. *J. Fluid Mech.* **474**, 299–318.
- WÄHLIN, A.K. 2002 Topographic steering of dense currents with application to submarine canyons. *Deep-Sea Res. Part I: Oceanogr. Res. Pap.* **49**, 305–320.
- WUNSCH, C. & FERRARI, R. 2004 Vertical mixing, energy, and the general circulation of the oceans. *Annu. Rev. Fluid Mech.* **36**, 281–314.